

THE REDSHIFT DEPENDENCE OF ALCOCK-PACZYNSKI EFFECT: COSMOLOGICAL CONSTRAINTS FROM THE CURRENT AND NEXT GENERATION OBSERVATIONS

XIAO-DONG LI¹, HAITAO MIAO¹, XIN WANG^{1,6}, XUE ZHANG², FENG FANG¹, XIAOLIN LUO¹, QING-GUO HUANG^{2,3,4,5}, MIAO LI¹

Draft version March 1, 2022

ABSTRACT

The tomographic Alcock-Paczynski (AP) test is a robust large-scale structure (LSS) measurement that receives little contamination from the redshift space distortion (RSD). It has placed tight cosmological constraints by using small and intermediate clustering scales of the LSS data. However, previous works have neglected the cross-correlation among different redshift bins, which could cause the statistical uncertainty being underestimated by $\sim 20\%$. In this work, we further improve this method by including this multi-redshifts full correlation. We apply it to the SDSS DR12 galaxies sample and find out that, for Λ CDM, the combination of AP with the Planck+BAO dataset slightly reduces (within $1-\sigma$) Ω_m to 0.304 ± 0.007 (68.3% CL). This then leads to a larger H_0 and also mildly affects $\Omega_b h^2$, n_s and the derived parameters z_* , r_* , z_{re} but not τ , A_s and σ_8 . For the flat w CDM model, our measurement gives $\Omega_m = 0.301 \pm 0.010$ and $w = -1.090 \pm 0.047$, where the additional AP measurement reduces the error budget by $\sim 25\%$. When including more parameters into the analysis, the AP method also improves the constraints on Ω_k , $\sum m_\nu$, N_{eff} by 20–30%. Early universe parameters such as $dn_s/d\ln k$ and r , however, are unaffected. Assuming the dark energy equation of state $w = w_0 + w_a \frac{z}{1+z}$, the Planck+BAO+SNIa+ H_0 +AP datasets prefer a dynamical dark energy at $\approx 1.5\sigma$ CL. Finally, we forecast the cosmological constraints expected from the DESI galaxy survey and find that combining AP with CMB+BAO method would improve the w_0 - w_a constraint by a factor of ~ 10 .

1. INTRODUCTION

The discovery of cosmic acceleration (Riess et al. 1998; Perlmutter et al. 1999) implies either the existence of a “dark energy” component in our Universe or the breakdown of general relativity on cosmological scales (see Yoo & Watanabe 2012, for a recent review). The theoretical explanation and observational probes of cosmic acceleration have attracted tremendous attention, and are still far from being well understood or accurately measured (Weinberg 1989; Li et al. 2011; Weinberg et al. 2013; Miao et al. 2018).

In an effort to probe the cosmic expansion history, large scale structure (LSS) surveys are utilized to extract information about two key geometrical quantities; the angular diameter distance D_A and the Hubble factor H . If they were precisely measured as functions of redshift, then tight constraints can be placed on cosmological parameters, like the matter density Ω_m and the equation of state (EoS) of dark energy w .

The Alcock-Paczynski (AP) test (Alcock & Paczynski 1979) provides a geometric probe of D_A and H . Given a certain cosmological model, the radial and tangential sizes of distance objects or structures can be computed as $\Delta r_{\parallel} = \frac{c}{H(z)} \Delta z$

and $\Delta r_{\perp} = (1+z)D_A(z)\Delta\theta$, where Δz , $\Delta\theta$ are the observed redshift span and angular size, respectively. When incorrect cosmological models are assumed for transforming galaxy redshifts into comoving distances, the wrongly estimated Δr_{\parallel} and Δr_{\perp} induces geometric distortion (see Figure 1). In galaxy redshift surveys, measuring the galaxy clustering in the radial and transverse directions enables us to probe the AP distortion, and thus place constraints on cosmological parameters (Ryden 1995; Ballinger, Peacock & Heavens 1996; Matsubara & Suto 1996; Outram et al. 2004; Blake et al. 2011; Lavaux & Wandelt 2012; Alam et al. 2016; Mao et al. 2016).

The main difficulty of AP test is that the radial distances of galaxies, inferred from their observed redshifts, are inevitably affected by the galaxy peculiar motions. This leads to apparent anisotropies in the clustering signal even if the adopted cosmology is correct. This effect, known as redshift-space distortions (RSD), is usually much more significant than the AP distortion, and is notoriously difficult to be accurately modeled in the statistics of galaxy clustering (Ballinger, Peacock & Heavens 1996; Jennings et al. 2011).

As a complementary method to apply the AP test, Marinoni & Buzzi (2010) proposed to statistically study a large number of galaxy pairs and search for the deviation from a symmetric distribution of direction; however, since the peculiar velocity distorts the observed redshifts and changes the apparent tilt angles of galaxy pairs, this method is also seriously limited by RSD (Jennings et al. 2011). In an effort to minimize RSD contamination, the shape of void regions (Ryden 1995; Lavaux & Wandelt 2012) has also been proposed as an AP probe. This approach has the advantage that the void regions are easier to model compared with dense regions, but has limitations in that it utilizes only low density regions of the LSS, and requires large samples to attain statistical significances and achieve competitive constraints (Mao et al. 2016).

Recently, a novel method of applying the AP test by investigating the *redshift dependence* of the distortion was proposed

lixiaod25@mail.sysu.edu.cn

Corresponding Author: zhangxue@itp.ac.cn

¹ School of Physics and Astronomy, Sun Yat-Sen University, Zhuhai 519082, P. R. China

² CAS Key Laboratory of Theoretical Physics, Institute of Theoretical Physics, Chinese Academy of Sciences, Beijing 100190, China

³ School of Physical Sciences, University of Chinese Academy of Sciences, No. 19A Yuquan Road, Beijing 100049, China

⁴ Synergetic Innovation Center for Quantum Effects and Applications, Hunan Normal University, 36 Lushan Lu, 410081, Changsha, China

⁵ Center for Gravitation and cosmology, College of Physical Science and Technology, Yangzhou University, 88 South University Ave., 225009, Yangzhou, China

⁶ Canadian Institute for Theoretical Astrophysics, 60 St. George St., Toronto, ON, M5H 3H8, Canada

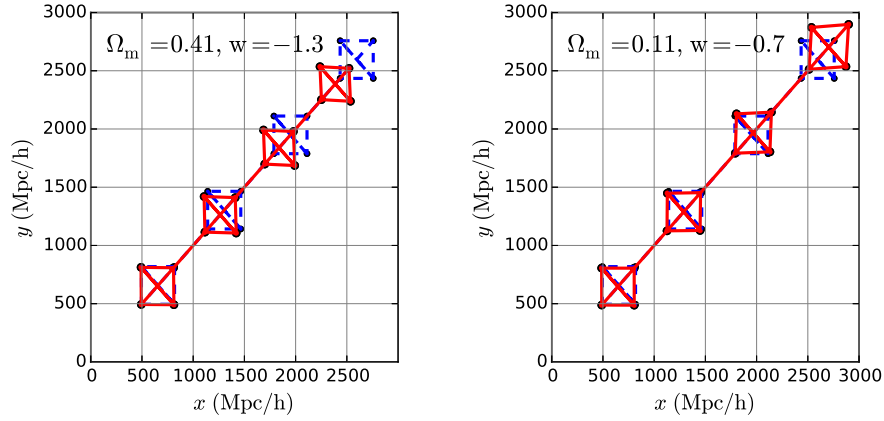


FIG. 1.— The AP distortion in two wrongly assumed cosmologies $\Omega_m = 0.41, w = -1.3$ and $\Omega_m = 0.11, w = -0.7$, for an observer whose true cosmology being $\Omega_m = 0.26, w = -1$. Four perfect squares are measured by the observer located at the origin. The apparently distorted shapes are plotted in red solid lines, while the underlying true shapes are plotted in blue dashed lines. The large redshift dependence of the distortion motivates us to conduct the *tomographic* analysis.

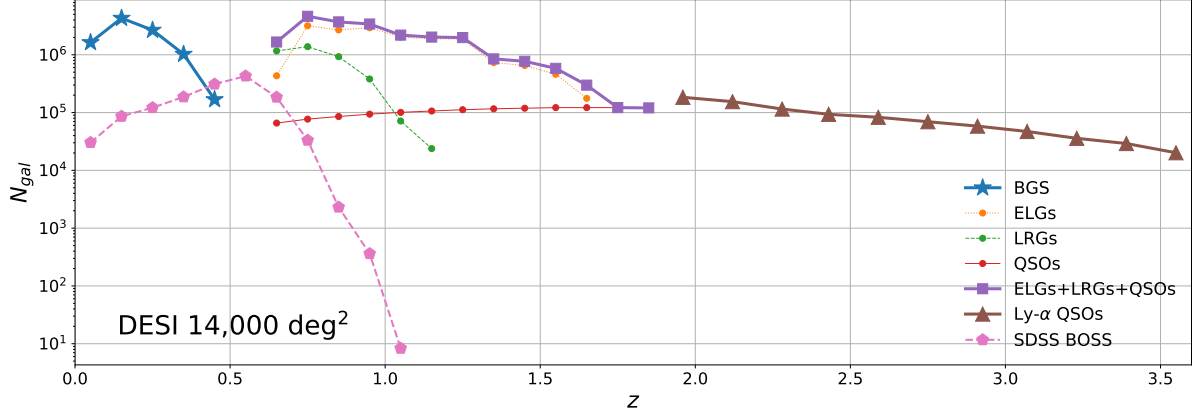


FIG. 2.— Expected redshift distribution of the galaxy sample from the DESI survey. We plotted the number of galaxies N_{gal} in 30 redshift bins. Among them, the 18 redshift bins of galaxies at $z \lesssim 1.9$ are used to forecast the performance of AP if applied to them. For comparison, the SDSS BOSS galaxies N_{gal} are also plotted.

by Li et al. (2014, 2015). The method is motivated by Park & Kim (2010), where the authors found adopting wrong set of cosmological parameters would produce redshift-dependent distortion in the LSS. Li et al. (2014, 2015) applied this idea to the AP test analysis. The authors found that, on one hand, the anisotropies produced by the RSD effect are, although large, maintaining a nearly uniform magnitude over a large redshift range; on the other hand, the degree of anisotropies produced by AP varies much more significantly. So they developed a method searching for the AP distortion from the redshift evolution of the anisotropies in LSS.

A consequence of reducing the RSD effect is that, by avoiding the complex modeling of galaxy position and velocity distributions, it becomes possible to use galaxy clustering on scales as small as $6\text{--}40 h^{-1}\text{Mpc}$. In this region, there exists a large amount of clustered structures (Zhang et al. 2018); thus enables us to derive tight constraint on cosmological parameters. This large amount of information can hardly be utilized by other LSS statistical methods.

The first application of this AP method (hereafter the tomographic AP method) to observational data was performed in Li et al. (2016). The authors split the 1.13 million Sloan Digital Sky Survey (SDSS) Data Release 12 (DR12) galaxies into six redshift bins, measured their anisotropic 2PCFs,

and quantified the redshift evolution of anisotropy. In combination with the datasets of Cosmic Microwave Background (CMB), type Ia supernovae (SNIa), baryon acoustic oscillations (BAO), and the H_0 measurements, the authors obtained $\Omega_m = 0.301 \pm 0.006$, $w = -1.054 \pm 0.025$ in a flat universe with cold dark matter and constant EoS dark energy components (hereafter $w\text{CDM}$). The error bars are reduced by as much as 40% by adding the AP method into the combination of CMB+SNIa+BAO+ H_0 .

As a follow-up study, Li et al. (2018) improved the method by developing a technique accurately approximating the 2PCFs in different cosmologies. This greatly reduces the computational expense of the 2PCFs, thus enables the exploration of models with three or more parameters. Li et al. (2018) applied the method to constrain a model of dynamical dark energy EoS $w(z) = w_0 + w_a \frac{z}{1+z}$ (hereafter $w_0w_a\text{CDM}$), and improved the Planck+BAO+SNIa+ H_0 constraint on $w_0\text{--}w_a$ by as much as 50%. Furthermore, in a very recent work, Zhang et al. (2018) combined the tomographic AP method with the BAO measurements, and obtained a Hubble constant $H_0 = 67.78^{+1.21}_{-1.86} \text{ km s}^{-1} \text{ Mpc}^{-1}$ (2.26% precision). The inclusion of AP reduces the error bar by 32%.

As a newly developed technique, the tomographic AP method shows promising potential in constraining cosmolog-

ical parameters. However, it is still far from becoming as mature as the BAO method. To summarize, the method needs to be improved in three aspects:

- We shall improve its methodology, by enhancing its statistical power, better understanding and estimating the systematical effects, and reducing the computational cost, etc.
- So far the method has only been used to constrain a limited set of parameters of Ω_m , $w(z)$ and H_0 . It is undoubtedly desirable to extend its application to more parameters and models.
- Given that there are many on-going and planned LSS surveys including DESI (Aghamousa et al. 2016), EUCLID (Laureijs et al. 2011), HETDEX (Hill et al. 2008)), it is necessary to forecast the constraining power when the method is applied to these surveys.

In this work we explored all these three issues. In Sec. 2, we showed that the methodology used in Li et al. (2014, 2015, 2016, 2018) neglected the correlations among different redshift bins, which leads to an over-estimation of statistical power and a large statistical fluctuation. We proposed a full covariance matrix approach to solve this problem and make the analysis statistically more perfect. In Sec. 3, we performed a comprehensive study on its constraints on a series of cosmological parameters. In Sec. 4, we forecast the cosmological constraints expected from the DESI survey. Conclusions of our work are given in Sec. 5.

2. DATA AND METHODOLOGY

The data and methodology used in this work is similar to what used in Li et al. (2014, 2015, 2016, 2018), except that we more completely evaluate the statistical uncertainties.

2.1. Data

2.1.1. SDSS DR12 Galaxies

The Sloan Digital Sky Survey (York et al. 2000), as the currently largest spectroscopic galaxy survey, has obtained spectra for more than three million astronomical objects. This created the most detailed three-dimensional maps of the Universe ever made. BOSS (Baryon Oscillation Spectroscopic Survey) (Dawson et al. 2012; Smee et al. 2013), as a part of the SDSS-III survey (Eisenstein et al. 2011), has obtained spectra and redshifts of 1.37 million galaxies selected from the SDSS imaging, covering a sky region of 9376 deg^2 and a redshift span of $0.1 \lesssim z \lesssim 0.75$. Its wide redshift coverage and large amount of galaxies makes it the best material for performing the tomographic analysis.

Following Li et al. (2016), we use the spectroscopic galaxy sample of SDSS-III BOSS DR12, containing the LOWZ catalogue at $0.1 \lesssim z \lesssim 0.45$ and the CMASS catalogue covering $0.4 \lesssim z \lesssim 0.7$ (Reid et al. 2016). For purpose of a tomographic clustering analysis, we split the sample into six, non-overlapping redshift bins of $0.150 < z_1 < 0.274 < z_2 < 0.351 < z_3 < 0.430 < z_4 < 0.511 < z_5 < 0.572 < z_6 < 0.693$ ⁷. The total number of galaxies used in the analysis is 1,133,326.

⁷ The boundaries are determined so that the number of galaxies are roughly the same in different redshift bins (for LOWZ and CMASS samples, respectively).

2.1.2. Horizon Run 4 mocks

We rely on the Horizon Run 4 (HR4; Kim et al. 2015) to estimate and correct the systematics. HR4 is a large N-body simulation with box size $L = 3150 h^{-1} \text{ Mpc}$ and number of particles 6300^3 , produced under the WMAP5 (Komatsu et al. 2011) cosmological parameters $(\Omega_b, \Omega_m, \Omega_\Lambda, h, \sigma_8, n_s) = (0.044, 0.26, 0.74, 0.72, 0.79, 0.96)$. Mock galaxy samples are then created using a modified version of the one-to-one correspondence scheme (Hong et al. 2016). Comparing the 2pCF of the mocks to the SDSS DR7 volume-limited galaxy sample (Zehavi et al. 2011), we found the simulated 2pCF shows a finger of god (FOG) feature (Jackson 1972) rather close to the observation. The projected 2pCF agrees with the observation within 1σ deviation on scales greater than $1 h^{-1} \text{ Mpc}$ Hong et al. (2016).

2.1.3. MultiDark PATCHY mocks

We utilize the set of 2,000 MultiDark PATCHY mock catalogues (Kitaura et al. 2015) from the dark matter simulation to the covariance matrix. The MultiDark PATCHY mocks are produced using approximate gravity solvers and analytical-statistical biasing models, calibrated to the BigMultiDark N-body simulation (Klypin et al. 2016). The mock surveys can well reproduce the number density, selection function, survey geometry, and 2PCF measurement of the BOSS DR12 catalogues, and have been adopted in a series of works (see Alam et al. 2016, and references therein) to conduct clustering analysis of BOSS galaxies.

2.1.4. DESI galaxies

The DESI Aghamousa et al. (2016) observational program is a future project measuring the baryon acoustic feature of the large-scale structure, as well as the distortions effects of redshift space. DESI provides high precision measurements of the Universe's expansion rate up to $z \sim 1.5$. The baseline assumption is that it runs over an approximately five years period covering $14,000 \text{ deg}^2$ in area. The DESI survey makes observations of four types of objects:

- A magnitude-limited Bright Galaxy Survey (BGS) ($0.05 < z < 0.45$) comprising approximately 10 million galaxies;
- Bright emission line galaxies (ELGs) (up to $z = 1.65$) probing the Universe out to even higher redshift;
- Luminous red galaxies (LRGs) (up to $z = 1.15$), which extend the BOSS LRG survey in both redshift and survey area;
- Quasi-stellar objects (QSOs) as direct tracers of dark matter in the redshift range $0.65 < z < 1.85$.

The number density distribution of these galaxies is shown in Figure 2. Our forecast in section 4. is based on these numbers.

2.2. Methodology

2.2.1. Quantifying the Anisotropy

Li et al. (2016) (hereafter Li16) split the BOSS DR12 galaxies into six redshift bins, and computed the integrated 2pCF in each bin

$$\xi_{\Delta s}(\mu) \equiv \int_{s_{\min}}^{s_{\max}} \xi(s, \mu) ds, \quad (1)$$

where the correlation function ξ is measured as a function of s , the distance separation of the galaxy pair, and $\mu = \cos(\theta)$, with θ being the angle between the line joining the pair of galaxies and the line of sight (LOS) direction to the target galaxy. The range of integration was chosen as $s_{\min} = 6 h^{-1}\text{Mpc}$ and $s_{\max} = 40 h^{-1}\text{Mpc}$. By focusing on the redshift dependence of anisotropy, the RSD effect is largely reduced, and it becomes possible to use the galaxy clustering down to $6 h^{-1}\text{Mpc}$.

To mitigate the systematic uncertainty from *galaxy bias* and *clustering strength*, Li16 further normalized the amplitude of $\xi_{\Delta s}(\mu)$ to focus on the shape, i.e.

$$\hat{\xi}_{\Delta s}(\mu) \equiv \frac{\xi_{\Delta s}(\mu)}{\int_0^{\mu_{\max}} \xi_{\Delta s}(\mu) d\mu}. \quad (2)$$

A cut $\mu < \mu_{\max}$ is imposed to reduce the fiber collision and FOG effects.

2.2.2. The Redshift Evolution of Anisotropy

The redshift evolution of anisotropy, between the i th and j th redshift bins are be quantified as

$$\delta\hat{\xi}_{\Delta s}(z_i, z_j, \mu) \equiv \hat{\xi}_{\Delta s}(z_i, \mu) - \hat{\xi}_{\Delta s}(z_j, \mu), \quad (3)$$

where the systematics of $\delta\hat{\xi}_{\Delta s}$ (hereafter $\delta\hat{\xi}_{\Delta s, \text{sys}}$), mainly comes from the redshift evolution of RSD effect⁸, was measured from the Horizon Run 4 (Kim et al. 2015) N-body simulation and subtracted.

2.2.3. “Part-cov” approach of likelihood

To quantify the overall redshift evolution in the sample, Li16 chose the *first redshift bin* as the reference, compare the measurements in higher redshift bins with it, and then sum up these differences. So we have the following χ^2 function describing the total of evolution

$$\chi_{\text{AP, part-cov}}^2 \equiv \sum_{i=2}^6 \sum_{j_1=1}^{n_\mu} \sum_{j_2=1}^{n_\mu} \mathbf{p}(z_i, \mu_{j_1}) (\mathbf{Cov}_i^{-1})_{j_1, j_2} \mathbf{p}(z_i, \mu_{j_2}), \quad (4)$$

where n_μ denotes the binning number of $\hat{\xi}_{\Delta s}(\mu)$, and $\mathbf{p}(z_i, \mu_j)$ is defined as

$$\mathbf{p}(z_i, \mu_j) \equiv \delta\hat{\xi}_{\Delta s}(z_i, z_1, \mu_j) - \delta\hat{\xi}_{\Delta s, \text{sys}}(z_i, z_1, \mu_j). \quad (5)$$

The covariance matrix \mathbf{Cov}_i is estimated from the 2,000 MultiDark-Patchy mocks (Kitaura et al. 2015). In wrong cosmologies, the AP effect produces large evolution of clustering anisotropy, thus would be disfavored due to a large χ^2 value.

In Eq.4 we labeled the χ^2 function by the χ^2 analysis by “part-cov”, to denote that this χ^2 analysis does not include the correlations among different $\mathbf{p}(z_i)$ s. The different $\mathbf{p}(z_i)$ s are actually correlated with other, in the sense that 1) since all the $\mathbf{p}(z_i)$ s takes the first redshift bin as the reference, the fluctuation in the first bin enters all $\mathbf{p}(z_i)$ s and makes them statistically correlate with each other; 2) the LSS at different redshift bins have correlations even if they are not overlapping with each other (galaxies lying near the boundary of a redshift bin have been affected by galaxies in the both nearby bins in the past structure formation era).

⁸ The redshift evolution of anisotropy from RSD is, in general, smaller than those from AP (Li et al. (2014, 2015)). But it still creates small redshift dependence in $\hat{\xi}_{\Delta s}(\mu)$ (Li et al. 2014, 2015).

We tested and found ignoring 2) does not lead to significant changes in the results, so it is a minor effect. But ignoring 1) leads to $\sim 20\%$ mis-estimation of the statistical error. The “part-cov” method relies on the first redshift bin as the reference. If this bin happened to have a large deviation (i.e. due to statistical fluctuation) from its statistical expectation, then all \mathbf{p} s would be affected. This creates statistical error in the results, which haven’t been included in Li et al. (2016, 2018).

Appendix A shows the mis-estimation and large fluctuation of this part-cov approach. They would be overcome if we include the correlations among the $\mathbf{p}(z_i)$ s into the analysis.

2.2.4. “Full-cov” approach of likelihood

We adopt the following formula to represent the χ^2 function including all correlations,

$$\chi_{\text{AP, full-cov}}^2 \equiv \mathbf{P} \cdot \mathbf{Cov} \cdot \mathbf{P}, \quad (6)$$

where

$$\mathbf{P} = (\tilde{\mathbf{p}}(z_2, \mu_{j_1}), \dots, \tilde{\mathbf{p}}(z_6, \mu_{j_1})), \quad (7)$$

a vector containing $(n_z - 1) \times (n_\mu)$ components, is built by joining all $\tilde{\mathbf{p}}(z_i, \mu_j)$ s together. Here we re-define the \mathbf{p} as the evolution between the *nearby redshift bins*, i.e.

$$\tilde{\mathbf{p}} \equiv \delta\hat{\xi}_{\Delta s}(z_i, z_{i-1}) - \delta\hat{\xi}_{\Delta s, \text{sys}}(z_i, z_{i-1}). \quad (8)$$

Actually, the results does not change if we still use the original \mathbf{p} defined in Eq(5)⁹. We redefine \mathbf{p} as $\tilde{\mathbf{p}}$ so that the formula explicitly has no special redshift bin chosen as the reference.

2.2.5. The covariance matrix

The covariance matrix \mathbf{Cov} , estimated from the MultiDark mocks, was shown in the Figure 3. The upper panel shows the covariance matrix when we split $\xi_{\Delta s}$ into 20 bins in μ space, while the lower panel shows the normalized covariance matrix (i.e. the correlation coefficient).

We find:

- Since we have 6 redshift bins, in total we need $6-1=5$ $\delta_{i,j}\xi_{\Delta s}$ s to characterize the evolution among them. So the plot of total covariance matrix contains $5 \times 5 = 25$ regions of “cells”.
- The five “diagonal cells” describe the 20×20 auto covariance matrix of $\delta_{i,j}\xi_{\Delta s}(\mu)$. μ -bins close to each other strong positive correlations, while μ -bins very far away from each other have negative correlations imposed by the normalization condition.
- The 20 “non-diagonal boxes” describe the cross-correlation among different $\delta_{i,j}\xi_{\Delta s}$ s. They have non-zero values.
- Those $\delta_{i,j}\xi_{\Delta s}$ s who have overlapping redshift bins are strongly correlated since they contain the same $\xi_{\Delta s}(\mu, z_i)$ (e.g., $\delta_{2,1}\xi_{\Delta s}$ and $\delta_{3,2}\xi_{\Delta s}$ both depend on the $\xi_{\Delta s}$). Their pattern of correlation is similar to the diagonal boxes, i.e. positive correlation among nearby μ -bins and negative among very faraway μ -bins.
- $\delta_{i,j}\xi_{\Delta s}$ s without any overlapping bins do not show significant cross-correlations (correlation coefficients close to 0). We tested and found that, ignoring them does not have statistically significant impact on the derived cosmological constraints.

⁹ Once we include the full covariance matrix, the result does change no matter how we *linearly transform* the \mathbf{p} s.

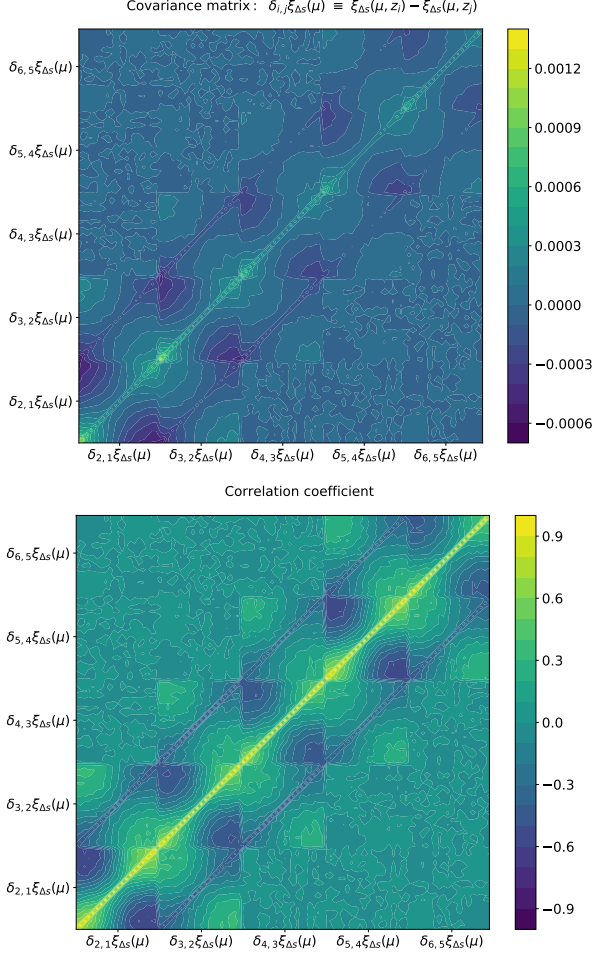


FIG. 3.— The covariance matrix of the $\hat{\xi}_{\Delta_s}(z_i, z_{i-1})$ s (upper panel), and its normalized version (i.e. correlation coefficients, lower panel). We split each $\hat{\xi}_{\Delta_s}(z_i, z_{i-1})$ into 20 bins in the μ space, so five of them form a 100×100 covariance matrix. The five 20×20 matrices at the diagonal are the auto-correlations, while the off-diagonal matrices describe the cross-correlation. The non-zero cross-correlation, especially between the $\hat{\xi}_{\Delta_s}(z_i, z_{i-1})$ s next to each other, suggests the necessity of including them into the analysis. See Section 2.2.4 for details.

3. COSMOLOGICAL CONSTRAINTS

The cosmological constraints are derived from the likelihood method described in Sec. 2.2. We divide our discussion into two sections. In Sec. 3.1 we presented the constraints on the *background parameters* of w , w_0 , w_a , Ω_m and H_0 , within the framework of Λ CDM, w CDM and $w_0 w_a$ CDM models, respectively. These parameters are *directly* constrained by the AP method, which measures the geometry of the universe in the late-time expansion era¹⁰. In Sec. 3.2, we extend the scope and explore the *other cosmological parameters*, including the Λ CDM parameters and their derivations, and the 1-parameter extensions to Λ CDM and w CDM models.

We present the cosmological constraints when the AP likelihood is combined with several external datasets, including the full-mission Planck observations of CMB temperature and polarization anisotropies (Ade et al. 2015), the BAO dis-

tance priors measured from SDSS DR11 (Anderson et al. 2013), 6dFGS (Beutler et al. 2011) and SDSS MGS (Ross et al. 2015), the “JLA” SNIa sample (Betoule et al. 2014), and the Hubble Space Telescope measurement of $H_0 = 70.6 \pm 3.3$ km/s/Mpc (Riess et al. 2011; Efstathiou 2014). They are exactly the same datasets used in Li et al. (2016, 2018).

3.1. Constraints on background parameters

Table 1 summarizes the Planck+BAO and Planck+BAO+AP constraints on the background parameters w , w_0 , w_a , Ω_m and H_0 , within the framework of Λ CDM, w CDM and $w_0 w_a$ CDM models. In what follows, we discuss about them in details.

3.1.1. Λ CDM parameters

The Λ CDM model with EoS $w_\Lambda = -1$ is the simplest candidate among a large number of dark energy models, with the Hubble parameter taking form of

$$H(z) = H_0 [\Omega_m (1+z)^3 + \Omega_\Lambda]^{1/2}, \quad (9)$$

where $\Omega_m + \Omega_\Lambda = 1$ (we neglect curvature and radiation). Although Λ CDM model seriously suffers from the theoretical fine tuning and coincidence problems (Weinberg 1989), it is in good agreement with most of the current observational data (Li et al. 2011).

Table 1 list the constraints on Ω_m , H_0 derived from Planck+BAO and Planck+BAO+AP, respectively. Including AP into the analysis leads to a $\lesssim 1\sigma$ shift in the central values of Ω_m , H_0 , i.e. from (0.310, 67.6) to (0.304, 68.1), respectively.

3.1.2. w CDM parameters

The simplest generalization to Λ is considering a constant dark energy EoS w , and the Hubble parameter is given by

$$H(z) = H_0 [\Omega_m (1+z)^3 + \Omega_{de} (1+z)^{3(1+w)}]^{1/2}, \quad (10)$$

where Ω_{de} is the current value of the dark energy density. If $w = -1$, then w CDM reduces to Λ CDM, with $\Omega_{de} = \Omega_\Lambda$.

The upper panel of Figure 4 illustrates the constraint on w from the combination of Planck+BAO, Planck+BAO+AP, Planck+BAO+SNIa+ H_0 +AP. The mean values as well as the 68% and 95% limits are

$$w = -1.031^{+0.067}_{-0.057} \quad \text{Planck+BAO}; \quad (11)$$

$$w = -1.089^{+0.040}_{-0.054} \quad \text{+AP}; \quad (12)$$

$$w = -1.054^{+0.046}_{-0.052} \quad \text{+SNIa+}H_0\text{+AP}. \quad (13)$$

If we describe the *decrement in the error bar* (or equivalently, improvement in the precision) by $\frac{\sigma_{w.o.AP} - \sigma_{with AP}}{\sigma_{w.o. AP}}$, then adding AP into the Planck+BAO combination reduces the errors by $\sim 30\%$. The inclusion of AP also shifts the constraint toward negative EoS by $\sim 1\sigma$, making the results marginally consistent with $w = -1$ in 2σ . Further adding the SNIa and H_0 “pulled back” it towards $w = -1$.

The lower panel of Figure 4 shows the marginalized constraint in the Ω_m - w plane. We see a positive degeneracy between the two parameters, and a shift of w towards negative values. Correspondingly, a smaller amount of Ω_m is preferred.

It is commonly believed that since the CMB data helps the BAO method to determine the absolute value of the sound horizon, tight constraints can be achieved if the two combined. So we will use Planck+BAO as a “standard combination” and check how much the constraints improve after

¹⁰ There is one exception. AP method alone can not put constraint on H_0 . The change in H_0 corresponds to a uniform re-scaling of LSS, and produces no anisotropy. But the AP method can improve its constraint by breaking its degeneracy with other parameters (Zhang et al. 2018).

TABLE 1
MEAN VALUES AND 68% CONFIDENCE LIMITS OF COSMOLOGICAL PARAMETERS FOR THE Λ CDM, w CDM AND w_0w_a CDM MODELS, FROM COMBINATIONS OF PLANCK+BAO AND PLANCK+BAO+AP. THE UNCERTAINTIES (OF THE LAST 2 DIGITS OF THE NUMBERS) ARE LISTED IN THE BRACKETS.

Model	Ω_m		H_0		w_0		w_a	
	Planck+BAO	+AP	Planck+BAO	+AP	Planck+BAO	+AP	Planck+BAO	+AP
Λ CDM	0.3102(64)	0.3041(67)	67.63(48)	68.08(52)				
w CDM	0.306(13)	0.293(10)	68.3 ± 1.5	69.8 ± 1.2	-1.031(63)	-1.090(47)		
w_0w_a CDM	0.351(29)	0.300(17)	64.0 ± 2.7	69.3 ± 1.7	-0.51(30)	-0.95(18)	-1.47(83)	-0.53(53)

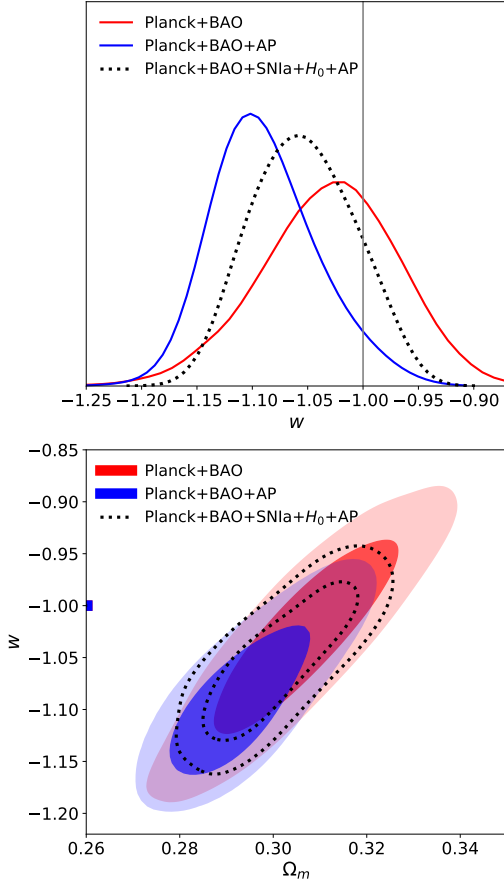


FIG. 4.— Cosmological constraints within the framework of w CDM. Upper panel: the constraint on w from the combinations of Planck+BAO, Planck+BAO+AP, Planck+BAO+SNla+ H_0 +AP. Lower panel: likelihood contours (68.3 and 95.4% CL) in the Ω_m - w plane.

adding AP. In fact, because CMB and AP constrain different epochs of expansion history, combining them can also effectively reduce the uncertainties of parameters. This can be seen from Figure 10 of Li et al. (2016), where we find the Planck and AP contours have orthogonal directions of degeneracy in the Ω_m - w space. Actually, combining these two constraints give

$$\Omega_m = 0.295 \pm 0.015, H_0 = 69.7 \pm 1.7, w = -1.08 \pm 0.05, \quad (14)$$

which are as tight as the Planck+BAO results.

The derived constrained from the full-covmat analysis is consistent with Li et al. (2016) except that here we obtained a larger error bar, mainly due to the inclusion of full covariance. A comparison between the two sets of results are presented in Appendix 5.

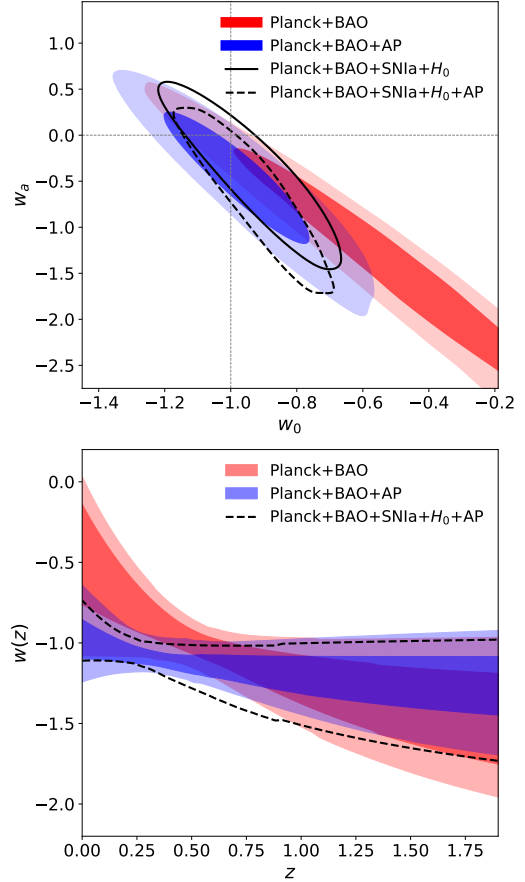


FIG. 5.— Cosmological constraints for w_0w_a CDM model. Upper panel: likelihood contours (68.3 and 95.4%) in the Ω_m - w plane. Adding AP into Planck+BAO greatly improves the constraints on the w_0 - w_a parameters. Low panel: evolution of $w(z)$ in the 68.3 and 95.4% CLs. A dynamical dark energy crossing $w = -1$ is mildly favored $\sim 1.5\sigma$ CL.

To ensure the robustness of the results, we have conducted a serious checks about the systematics and the options of the AP analysis. We do not find any statistically significant effect on the derived results. These tests are briefly discussed in Appendix 5.

3.1.3. w_0w_a CDM parameters

We move on to a further generalization and consider a dynamical EoS depend on z . As a simplest parameterization widely used in the literature, one can consider the 1st order Taylor expansion of w_{de} with respect to $(1-a)$, i.e.

$$w_{de}(z) = w_0 + w_a(1-a) = w_0 + w_a \frac{z}{1+z}, \quad (15)$$

which is the well-known Chevallier-Polarski-Linder (CPL) parameterization proposed by Refs. Chevallier & Polarski (2001); Linder (2003). The Hubble parameter is

$$H(z) = H_0[\Omega_m(1+z)^3 + \Omega_{de}(1+z)^{3(1+w_0+w_a)}e^{-3\frac{w_0 z}{1+z}}]^{1/2}. \quad (16)$$

Figure 5 shows the constraints on this dynamical dark energy model. The Planck+BAO combination can not lead to effective constraints on the w_0 - w_a parameters. We only obtain two weak bounds of $w_0 > -1.2$, $w_a < 0.5$ (95%), and the upper bound of w_0 and lower bound of w_a is left unconstrained. Adding AP closes the constraints and yields to

$$\begin{aligned} w_0 &= -0.95^{+0.13}_{-0.18} {}^{+0.35}_{-0.35}, \\ w_a &= -0.53^{+0.57}_{-0.43} {}^{+1.08}_{-1.17} \text{ Planck + BAO + AP.} \end{aligned} \quad (17)$$

The result is consistent with $w(z) = -1$ in 1σ . This manifests the power of AP method. Combining it with BAO significantly increases the amount of information extracted from the LSS data, and greatly tightens the dark energy constraint.

When further considering the SNIa and H_0 datasets, we find

$$\begin{aligned} w_0 &= -0.94^{+0.11}_{-0.11} {}^{+0.22}_{-0.21}, \\ w_a &= -0.38^{+0.45}_{-0.39} {}^{+0.82}_{-0.87} \\ &\quad (\text{Planck + BAO + SNIa} + H_0); \end{aligned} \quad (18)$$

$$\begin{aligned} w_0 &= -0.93^{+0.09}_{-0.10} {}^{+0.20}_{-0.18}, \\ w_a &= -0.65^{+0.45}_{-0.40} {}^{+0.83}_{-0.88} \\ &\quad (\text{Planck + BAO + SNIa} + H_0 + \text{AP}). \end{aligned} \quad (19)$$

The main effect of adding AP is a $\approx 0.7\sigma$ shift of w_a towards negative values (which can be seen evidently from the upper panel of Figure 5). As a result, a dynamical dark energy (i.e., $w_a \neq -1$) is preferred at $\approx 1.5\sigma$. The lower panel of the Figure shows that, the dark energy EoS is evolving from < -1 to > -1 from high redshift epoch to the present. $w = -1$ is consistent with the constraint at 2σ CL¹¹.

3.2. Constraints on the other cosmological parameters

3.2.1. Λ CDM parameters

Table 2 summarizes the Λ CDM parameters (6 basic parameters, 21 derived; see Ade et al. (2015) for the explanation of their meanings) constrained by Planck+BAO and Planck+BAO+AP combinations.

In the Λ CDM framework, adding AP into the analysis only affects the constraint on Ω_m . The matter amount Ω_m changes from 0.310 to 0.304, which is a 1.0σ CL drop (hereafter we use the Planck+BAO error bar to quantify the CLs of the changes). This then affects the constraints on many other parameters via the degeneracy among the parameters. For the basic parameters, we find¹²:

- The cold dark matter density $\Omega_c h^2$ also decreases by 1.0σ .
- The baryon ratio $\Omega_b h^2$ is increased by 0.5σ , which should come from the increasing of H_0 .

¹¹ In comparison, Li et al. (2018) found adding AP into Planck+BAO+SNIa+ H_0 leads to a dynamical dark energy at $\approx 1\sigma$ CL together with 50% reduction of w_0 - w_a parameter space.

¹² The uncertainties of some parameters become larger after AP is additionally combined. This is due to the tension between the AP and Planck+BAO datasets. The inclusion of AP can create a bi-peak PDF (probability density function) and the uncertainty is slightly increased (the existence of the second peak widens the 68.3% CL region).

TABLE 2
MEAN VALUES AND 68% CONFIDENCE LIMITS OF COSMOLOGICAL PARAMETERS FOR THE BASE Λ CDM MODEL FROM PLANCK+BAO AND PLANCK+BAO+AP COMBINATIONS. THE UNCERTAINTIES (OF THE LAST 2 DIGITS OF THE NUMBERS) ARE LISTED IN THE BRACKETS.

Parameter	Λ CDM	
	Planck+BAO	+AP
$\Omega_b h^2$	0.02228(14)	0.02235(14)
$\Omega_c h^2$	0.1189(10)	0.1179(12)
$100\theta_{MC}$	1.04081(31)	1.04093(32)
τ	0.081(17)	0.086(17)
$\ln(10^{10} A_s)$	3.094(33)	3.102(33)
n_s	0.9669(39)	0.9695(39)
H_0	67.63(48)	68.08(52)
Ω_Λ	0.6898(64)	0.6959(78)
Ω_m	0.3102(64)	0.3041(68)
$\Omega_m h^2$	0.14182(98)	0.14092(10)
$\Omega_m h^3$	0.09591(30)	0.09594(30)
σ_8	0.829(13)	0.829(14)
$\sigma_8 \Omega_m^{0.5}$	0.4615(88)	0.4572(89)
$\sigma_8 \Omega_m^{0.25}$	0.618(10)	0.616(11)
z_{re}	$10.17^{+1.56}_{-1.38}$	$10.56^{+1.58}_{-1.37}$
$10^9 A_s$	2.208(72)	2.225(75)
$10^9 A_s e^{-2\tau}$	1.877(11)	1.873(11)
Age/Gyr	13.806(22)	13.790(23)
z_*	1089.94(23)	1089.76(24)
r_*	144.79(24)	144.98(26)
$100\theta_*$	1.04100(30)	1.04112(32)
z_{drag}	1059.64(30)	1059.75(30)
r_{drag}	147.49(25)	147.66(26)
k_D	0.14038(29)	0.14025(30)
z_{eq}	3374(24)	3352(25)
k_{eq}	0.010297(72)	0.010231(77)
$100\theta_{s,eq}$	0.4520(23)	0.4541(25)

- The scalar spectral index n_s , which has negative degeneracy between $\Omega_c h^2$, is decreased by 0.7σ .
- The Thomson scattering optical depth due to reionization, τ , and the log power of the primordial curvature perturbations, $\ln(10^{10} A_s)$, has little degeneracy with the above parameters. So they are less affected (change $< 0.3\sigma$).

This leads to a serious of changes in the derived parameters:

- Due to the negative degeneracy between Ω_m and H_0 , the latter increased by 0.9σ .
- σ_8 is negatively correlated with both Ω_m and H_0 ; as a net effect, its value remains unchanged.
- The acoustic scale $100\theta_*$, crucially determined by the CMB angular power spectrum measurement, remains less affected.
- The z_* and r_* , affected by the density of energy components, are decreased and increased by 0.8σ ; similar

TABLE 3
CONSTRAINTS ON 1-PARAMETER EXTENSIONS TO THE Λ CDM AND w CDM MODELS, FOR COMBINATIONS OF PLANCK+BAO AND PLANCK+BAO+AP.
NOTE THAT WE QUOTE 95% LIMITS HERE.

Parameter	Λ CDM extension		w CDM extension	
	Planck+BAO	+AP	Planck+BAO	+AP
Ω_k	$-0.0002^{+0.0041}_{-0.0040}$	$0.0004^{+0.0042}_{-0.0039}$	$-0.0010^{+0.0066}_{-0.0061}$	$-0.0015^{+0.0042}_{-0.0044}$
$\sum m_\nu$ [eV]	< 0.181	< 0.141	< 0.295	< 0.243
N_{eff}	$2.97^{+0.34}_{-0.34}$	$3.07^{+0.33}_{-0.33}$	$2.95^{+0.38}_{-0.37}$	$2.96^{+0.37}_{-0.35}$
$dn_s/d\ln k$	$-0.0023^{+0.0132}_{-0.0138}$	$-0.0025^{+0.0133}_{-0.0136}$	$-0.0024^{+0.0134}_{-0.0136}$	$-0.0025^{+0.0132}_{-0.0139}$
r	< 0.115	< 0.121	< 0.113	< 0.111

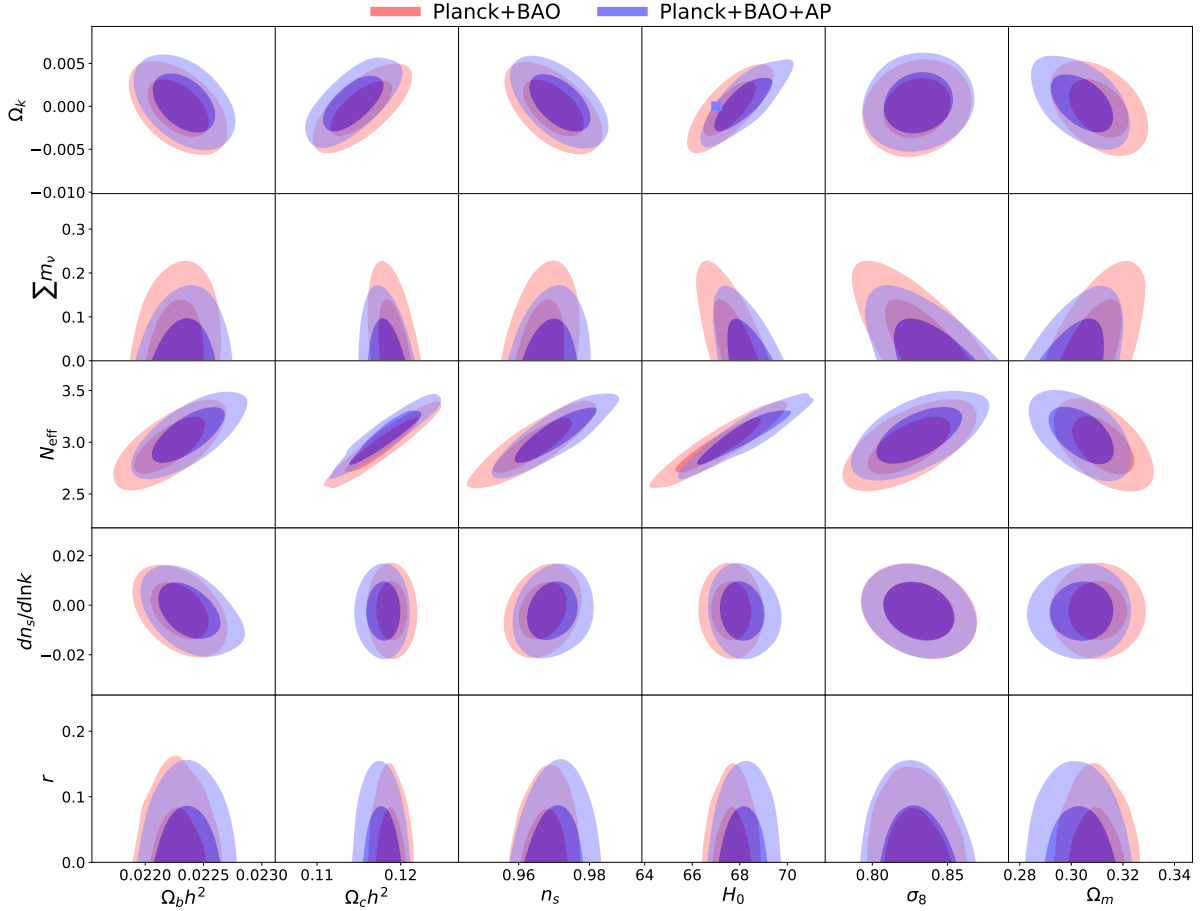


FIG. 6.— 68% and 95% confidence regions on 1-parameter extensions of the base Λ CDM, for Planck+BAO (red) and Planck+BAO+AP (blue).

effects are found for z_{drag} and r_{drag} .

- The change in Ω_m and H_0 leads to corresponding change in the combinations of Ω_Λ , $\Omega_m h^2$, $\sigma_8 \Omega_m^{0.5}$, and $\sigma_8 \Omega_m^{0.25}$. The only exception is $\Omega_m h^3$; its value is almost fully determined by the acoustic scale θ_* , so it remains unchanged.
- The age of the universe is rather sensitive to Ω_m and Ω_Λ ; we find it decreased by 0.7σ .
- The matter-radiation equality redshift z_{eq} drops by 0.9σ ,

i.e. happens in latter epoch. It is due to the drop in Ω_m and increment in radiation density Ω_r (because of larger h).

- Affected by z_{eq} and the fraction of energy components, $k_{\text{eq}} \equiv a(z_{\text{eq}})H(z_{\text{eq}})$ and $\theta_{s,\text{eq}} \equiv r_s(z_{\text{eq}})/D_A(z_{\text{star}})$ (the co-moving wavenumber of perturbation mode that entered Hubble radius at z_{eq} , and the angular scale of the sound horizon at z_{eq}) are also changed by 0.9σ .
- The characteristic wavenumber for damping k_D (which determines the photon diffusion length), whose value is

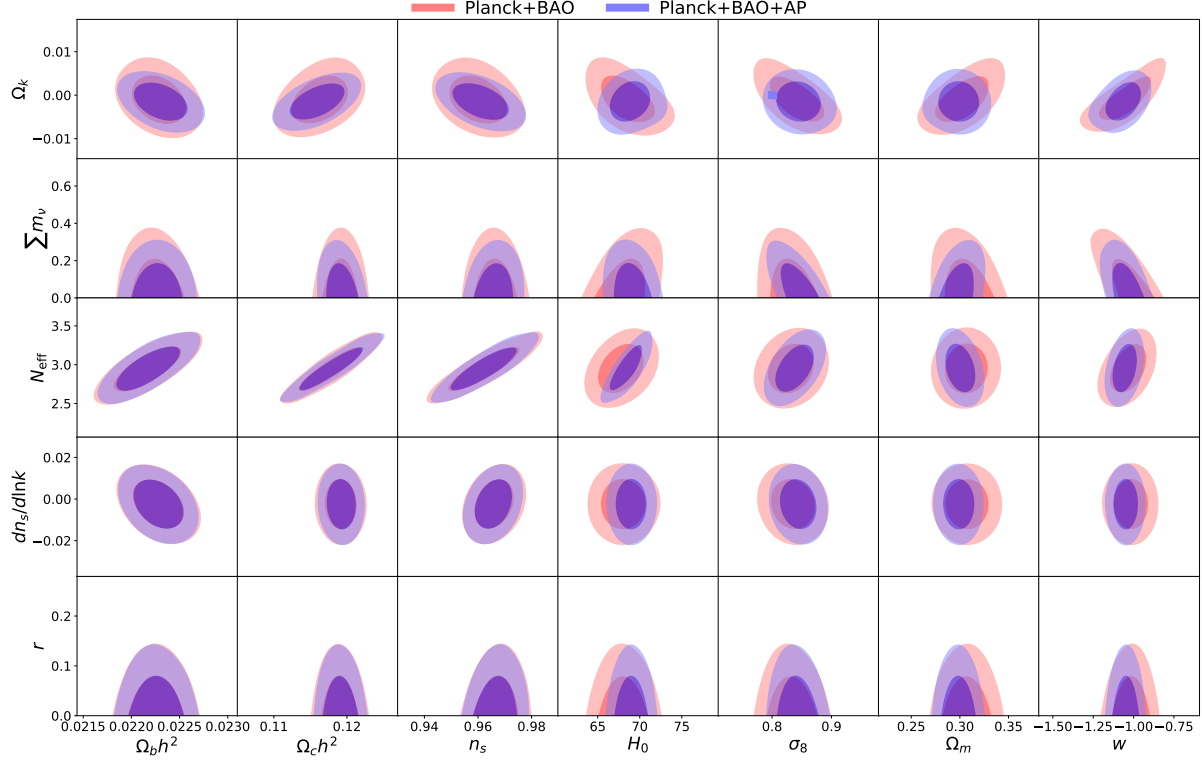


FIG. 7.— 68% and 95% confidence regions on 1-parameter extensions of the w CDM, from Planck+BAO (red) and Planck+BAO+AP (blue).

related to the fraction of energy components, is slightly changed by 0.4σ .

- Parameters directly determined by τ and A_s , including $10^9 A_s$, the parameter $10^9 A_s e^{-2\tau}$ describing small-scale damping of CMB due to Thomson scattering at reionization, and the reionization redshift z_{re} , all remain less affected.

3.2.2. 1-Parameter Extensions to Λ CDM and w CDM

The Planck+BAO and Planck+BAO+AP constraint on other parameters of one-parameter extensions to Λ CDM and w CDM cosmology are given in Table 3. The determination of uncertainty listed in the table are at a confidence level of 95%.

In this case, adding AP into the combination decreases the value of Ω_m , pulls the constrained region of w to slightly negative values, and also reduces its error bar by 30%. This leads to evident effect on the curvature Ω_k , the summation of neutrino mass $\sum m_\nu$, and the effective number of relativistic degrees of freedom in the Universe, N_{eff} , via their degeneracies with Ω_m and w . The early universe parameters, such as the running $dn_s/d\ln k$ and the tensor-to-scalar ratio r , are less affected.

- Due to the degeneracy in their roles of governing the cosmic distances, Ω_k is negatively correlated with Ω_m and positively correlated with w . As shown in Table 3, after considering AP the absolute value of Ω_k increases (0.28σ) changes the sign from minus to plus for the Λ CDM extension model. For w CDM extension model, the absolute value of Ω_k becomes bigger

(0.14σ), but the error is more tightly constrained (32% improvement).

- Using the AP effect the upper limit of the total neutrino mass are both reduced (by 22% and 18%) for Λ CDM extension and w CDM extension cases.
- By comparing two scenarios of Planck+BAO and Planck+BAO+AP datasets, N_{eff} is increased (0.6σ for Λ CDM extension, not obvious in case of w CDM extension). The reduction in the error of N_{eff} is small (from 11.4% to 10.7% for Λ CDM extension, and from 12.7% to 12.1% for w CDM extension).
- The running of the spectral index $dn_s/d\ln k$ is typically small, while the error is not significantly changed in both cases.
- Adding the AP test, it appears that the tensor-to-scalar ratio r is widely constrained for Λ CDM extension, and has tighter constraints for Λ CDM extension; but considering the statistical significance (0.05σ and 0.02σ), the effect is really ignorable.

The contour plots of one-parameter extensions to the Λ CDM model for combinations of Planck+BAO and Planck+BAO+AP are illustrated in Figure 6. We see clearly that combining the AP method increases the mean values of N_{eff} , $\Omega_b h^2$, n_s , H_0 , decreases $\Omega_c h^2$, Ω_m , noticeably reduced the errors of $\sum m_\nu$.

The contour plots of one-parameter extensions to the w CDM model are illustrated in Figure 6. In this case adding

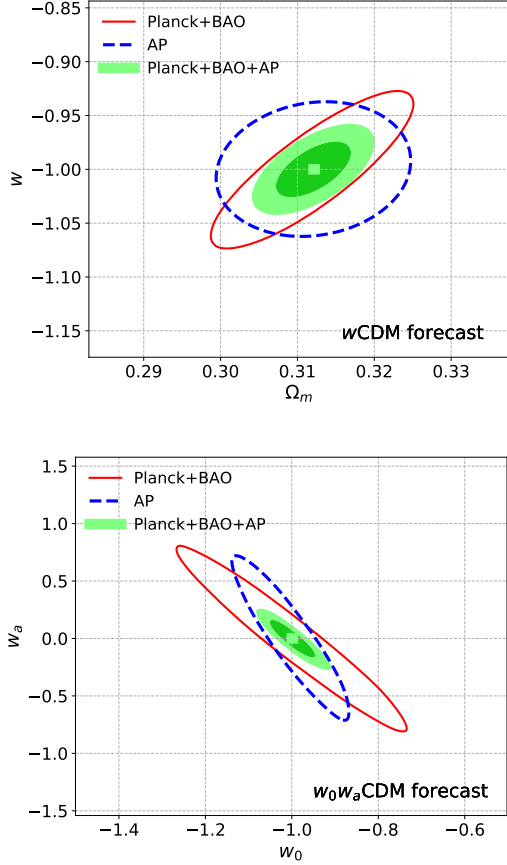


FIG. 8.— Expected constraints on w CDM and w_0w_a CDM models from DESI survey. Combining AP with Planck+BAO breaks the degeneracy between parameters, so reduces the uncertainty of w by 50%, and improving the w_0 - w_a constraint by a factor of 10.

AP helps sharpen the constraints Ω_k , $\sum m_\nu$, H_0 , σ_8 , Ω_m , w by 20-30%.

4. FORECAST

The number distribution of DESI galaxies is shown in Figure 2. Predicted constraints are made for the w CDM and w_0w_a CDM.

Estimating the covariance matrix of our correlation-based estimator is a complicated job (Bernstein 1994; O’Connell et al. 2016). Among various terms that scale differently with N_{gal} , we found that

$$\text{Cov} \propto 1/N_{gal}, \quad (20)$$

where N_{gal} is the number of galaxies, is already a good approximation. In Appendix 5 we tested it using SDSS galaxies and find its error is $\lesssim 1.5\% - 6\%$.

The DESI covariance matrices are then obtained simply using Eq. (20). Firstly, the covariance matrix of $\hat{\xi}_{\Delta s}(z_2, z_1, \mu)$ using SDSS galaxies are computed using the 2,000 MD-PATCHY mocks. We then choose this matrix as the baseline, take a ratio of the N_{gal} s of SDSS and DESI, and multiply this matrix by a factor to get the DESI covariance matrix¹³.

¹³ We take the SDSS galaxies in redshift bins 1,2 as the baseline to infer the DESI covariance matrices in all redshift bins. The results are rather insensitive to the redshifts of the baseline galaxies.

The contour plot of $\Omega_m - w$ in the w CDM model are illustrated at the top panel of Figure 8, using joint datasets of Planck+BAO, AP and Planck+BAO+AP, respectively. In the lower panels we show the contour plots of $w_0 - w_a$ in the frame of w_0w_a CDM model. In all cases we find that the constraint greatly reduced after adding the AP method.

For the constraint on a single parameter, the performance of AP and Planck+BAO are comparable to each other. If considering the joint constraint on two or more parameters, then the different directions of degeneracy from the two sets of results suggests that a greatly improved constraint can be achieved by combining them together.

In w CDM, adding AP reduces the constrained parameter space by 50%, achieving a precision of

$$\delta\Omega_m \approx 0.003, \delta w \approx 0.015 \text{ (Planck+DESI BAO+DESI AP)}. \quad (21)$$

In w_0w_a CDM, the addition of AP greatly reduces the constrained region by a factor of 10, achieving a precision of

$$\delta w_0 \approx 0.035, \delta w_a \approx 0.11 \text{ (Planck+DESI BAO+DESI AP)}. \quad (22)$$

5. CONCLUDING REMARKS

We conduct a comprehensive study about the cosmological constraints derived from tomographic AP method. Based on Li et al. (2014, 2015, 2016, 2018), we improve the methodology by including the full covariance among clustering in all redshift bins. We then apply it to current and future observational data.

When applying it to current observational data, we find:

- The AP method noticeably improves the constraints on background evolution parameters Ω_m , H_0 , w , w_0 , w_a . When combined it with the Planck+BAO the parameters’ error bars are reduced by $\sim 20 - 50\%$ (depends on the model and parameter).
- Using Planck+BAO+SNIa+ H_0 +AP, a dynamical dark energy $w_a \neq -1$ is preferred at $\approx 1.5\sigma$ CL.
- In the framework of Λ CDM, adding AP into Planck+BAO yields to a slightly smaller $\Omega_m = 0.301 \pm 0.010$, and a slightly larger $H_0 = 68.9 \pm 1.2$. This leads to $\lesssim 1\sigma$ changes in $\Omega_b h^2$, n_s , z_* , r_* , z_{re} , τ , A_s , σ_8 are less affected.
- When considering 1-parameter extensions to Λ CDM and w CDM models, we get improved constraints on Ω_k , $\sum m_\nu$, N_{eff} when combining AP with Planck+BAO. Since AP only puts constraints on the late time expansion, early universe parameters $dn_s/d\ln k$ and r are less affected.

We make a forecast of the w CDM and w_0w_a CDM constraints expected from Planck+DESI. We find the AP’s constraints on Ω_m , w , w_0 and w_a are as tight as the Planck+BAO ones, while the directions of degeneracy from the two differ from each other. Thus, combining them significantly improves the power of constraint. Adding AP reduces the error bar of w by 50%, and improving the w_0 - w_a constraint by a factor of 10.

It should be pointed out that the many results presented in this work are *not* the optimistic ones. We expect the result being further improved with the improvement in the methodology, e.g. optimistic binning scheme of the galaxies, more

aggressive clustering scales, more precise estimation of the covariance matrix, and so on.

According to our tests, for current surveys the systematic effects can not significantly affect the derived cosmological constraints. But it remains to be seen if this is true for future galaxy surveys. In particular, the systematic effects are estimated using one set of simulation performed in a fiducial cosmology, so the cosmological dependence of the systematics remains to be investigated in future works. It could be solved by, e.g. interpolating among systematics estimated from several sets of simulations with different cosmologies, considering theoretical estimation of systematics, and so on.

The tomographic AP method is so far the best method in separating the AP signal from the RSD distortions and using it we already achieved strong cosmological constraints. It is among the most powerful methods which can extract information from the $<40 h^{-1}\text{Mpc}$ small-scale clustering region. It is essentially important for us to improving this method and preparing for its application to the next generation surveys.

APPENDIX A: THE FULL COVMAT METHOD COMPARED WITH THE OLD METHOD

As described in Sec. 2, if one were ignoring the correlations between different $\delta_{i,j}\xi_{\Delta s}$ s, and simply using Eq. 4 to calculate the χ^2 , the result suffers from two problems:

- The statistical power is over-estimated since part of the correlations are not considered;
- The result has a special dependence on the choice of the redshift bin (here the 1st bin), and thus suffers from large statistical fluctuation.

Here we conduct a simple test to see how large the above two effects are. We simply consider six independent variables obeying normal distribution, who share the same variance but have different mean values:

$$X_i \sim \mathcal{N}(\mu = 10i, \sigma^2 = 1), \quad i = 1, 2, 3, 4, 5, 6. \quad (23)$$

We then use the ideas of Eq. (4,6) to define a χ^2 function characterizing the evolution among them:

$$\chi_1^2 \equiv \sum_{i=2}^6 (X_i - X_1)^2 / (\sigma^2 + \sigma^2), \quad (24)$$

$$\chi_2^2 \equiv \sum_{i=2}^6 \sum_{j=2}^6 (X_i - X_1) \text{Cov}_{i,j} (X_j - X_1), \quad (25)$$

and here the covariance matrix simply takes the form of

$$\text{Cov}_{ii} = 2; \text{Cov}_{ij} = 1 \text{ for } i \neq j. \quad (26)$$

We generate 10^6 sets of X_i , compute their χ^2 values, and plot the result in Figure 9. The mean and root-mean-square are listed in the legend. We find that

- In this case, the part-cov approach overestimates the χ^2 value by 57%; i.e., it over estimates the statistical significance of the evolution.
- The statistical fluctuation of the χ^2 derived from the part-cov approach is twice as large as the full-cov approach. This may lead to large bias when adopting this method to constrain cosmological parameters.

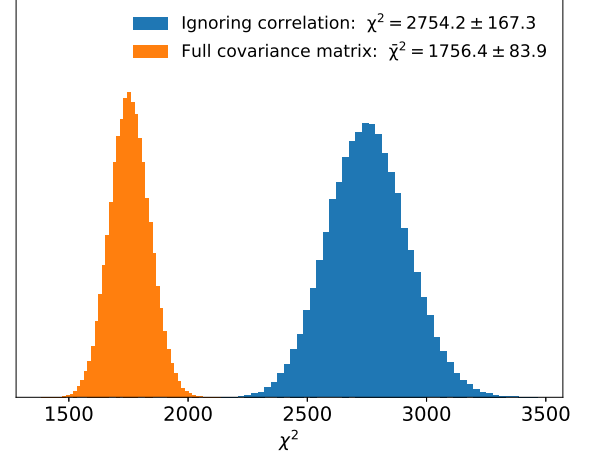


FIG. 9.— Histogram of χ^2 values using six test variables as described in Section 5. The full covariance matrix method results in reliable and stable estimation of χ^2 s, while ignoring the covariance overestimates the χ^2 s and suffers from significantly larger uncertainty.

Figure 10 compares the Planck+BAO+AP constraint on w CDM derived using the 1st-bin approach Eq. (yellow dashed line) and the full-covmat approach (blue line). We find

$$w = -1.068^{+0.036}_{-0.040}^{+0.076}_{-0.073} \text{ par-cov}, \quad (27)$$

$$w = -1.089^{+0.040}_{-0.054}^{+0.104}_{-0.088} \text{ full-cov}. \quad (28)$$

When using the full-covmat approach, the mean value was shifted towards the negative values by 0.02 ($\sim 0.4\sigma$), and the upper/lower error bars are enlarged by 10%/26%, respectively. The two sets of results are, still, in statistical consistency. The errors due to the defect of the 1st-bin approach are not serious.

The part-cov constraint is weaker than what reported in Li et al. (2015) ($w = -1.054 \pm 0.025$) because the difference in the choices of n_μ (Li et al. 2015) adopted $n_\mu = 6-40$ and here we reduced it to 20-25). Different from Li et al. (2015), in this work, we adopt the technique developed in Li et al. (2018) to efficiently approximate the 2PCFs in different cosmologies, and increase the size of covariance matrix from $n_\mu \times n_\mu$ to $5n_\mu \times 5n_\mu$. Both changes make the analysis more sensitive to the noise in the 2PCFs. So we reduce the number of binning to reduce the noise in $\xi_{\Delta s}$, which increase the reliability of the results, in the cost of scarifying some power of constraints.

APPENDIX B: ROBUSTNESS CHECK

Li16 tested the robustness of the tomographic AP method in details, and found the derived constraints on w CDM are insensitive to the adopted options within the range of $s_{\min} = 2-8 h^{-1} \text{Mpc}$, $s_{\max} = 30-50 h^{-1} \text{Mpc}$, $\mu_{\max} = 0.85-0.99$, and number of binning $n_\mu = 6-40$. Li et al. (2018) re-conducted the above tests in the $w_0 w_a$ CDM and obtained similar result. In what follows, we adopt the procedure of these two papers and test the robustness of the result. Our default set of options are $s_{\min} = 6 h^{-1} \text{Mpc}$, $s_{\max} = 40 h^{-1} \text{Mpc}$, $\mu_{\max} = 0.97$, and $n_\mu = 15-20$ ¹⁴.

¹⁴ Our n_μ is smaller than the default choice of Li16 (where they more ambitiously chose $n_\mu = 20-35$); this weakens the constraints by a little bit, but increases the robustness of the results, and also reduces the noise in the likelihood.

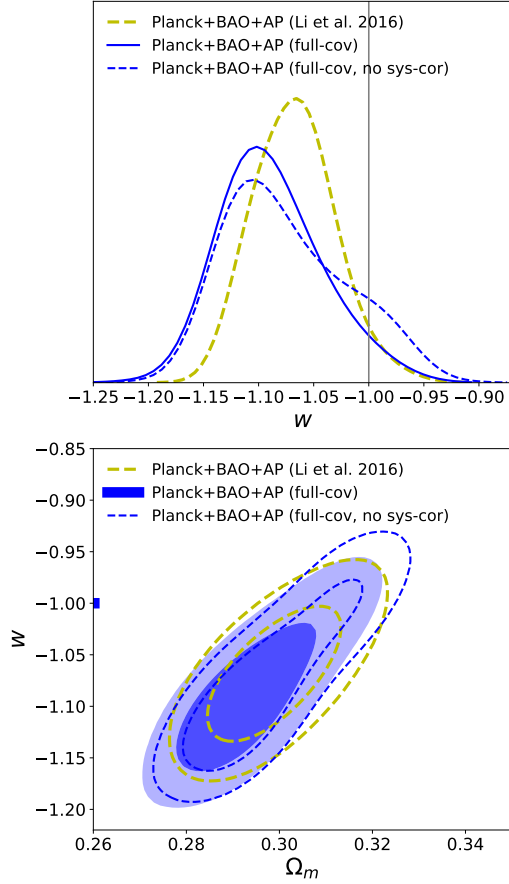


FIG. 10.— w CDM. 1) The method we used in this paper (full covmat method) is different from Li et al. 2016 (where they do not use full covmat). Result is slightly different. 2) If we discard systematic correction (estimated from HR4 simulation), there is minor change in the results.

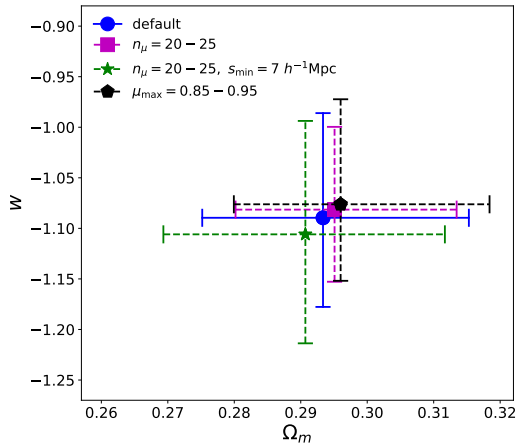


FIG. 11.— w CDM. Plotted are 2σ regions of parameters. If we change the options in the analysis, changes in the results are minor.

In the two panels of Figure 10 we also plotted the results without conduction any systematics (blue dashed). We see the peak value of w remain almost unchanged; the only effect is a small ($\sim 10\%$ for the 95% contour) enlargement of constrained region towards the larger value of w and Ω_m . This is similar to what we found in Li et al. (2018), i.e. for the analysis of current observations the systematics effect is not

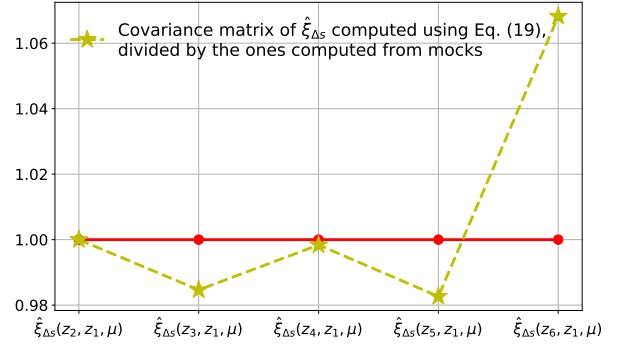


FIG. 12.— A rough check of Eq. (20) using 6 bins of SDSS DR12 galaxies (see Figure 2 of Li16). The covariance matrices of $\hat{\xi}_{\Delta s}(z_i, z_1, \mu)$, $i = 1, 2, 3, 4, 5$ are computed using two methods: 1. Measuring the scattering of $\delta_{i,j}$ from the 2,000 MultiDark-Patchy mocks, as we did in Li et al. (2016). 2. Measuring $\delta_{2,1}$ from the mocks, and infer the other $\delta_{i,j}$ s simply using Eq. (20). The y-axis shows the ratio between the results of the two methods (method 2 over method 1). We find the estimation (method 2) achieve $< 2\%$ precision for $\delta_{3,1}$, $\delta_{4,1}$, $\delta_{5,1}$. In the related redshift bins (redshift bins 1-5), the galaxy number density \bar{n}_{gal} varies in the range of $2 - 7 \times 10^{-4} h^{-1} \text{Mpc}^{-3}$ (as large as ~ 3 times). Given such a large fluctuation of \bar{n}_{gal} , Eq. (20) still achieves good precision. In the sixth bin \bar{n}_{gal} drops to significantly lower density ($1 \times 10^{-4} (h^{-1} \text{Mpc})^{-3}$, ~ 5 times lower than the first and second bins), while the error of method 2 is still $\lesssim 6\%$.

large enough to result in a statistically significant change of the results.

As a detailed test of the options adopted in the analysis, Figure 11 shows the mean values and 95% limits of the parameters, in cases of using a more aggressive binning scheme $n_\mu = 20 - 25$, a more conservative small-scale cut $s_7 = h^{-1} \text{Mpc}$, and a more conservative cut of correlation angle $\mu_{\text{max}} = 0.85 - 0.95$. In all cases we find rather small change in the mean values ($\lesssim 0.2\sigma$) and the limits ($\lesssim 15\%$). So we conclude the cosmological constraints obtained from the AP method does not sensitively depend on these options.

Finally, we test precision of Eq. 20 on the BOSS galaxies, and found it works with satisfying precision (Figure 12). The difference between the covariance matrices estimated from Eq. 20 and those directly computed using the mocks is $\lesssim 5\%$.

ACKNOWLEDGMENTS

We acknowledges the usage of Horizon Run simulations and MultiDark-Patchy mocks. We thank Zhiqi Huang and Xin Zhang for helpful discussions. XDL gratefully acknowledge professor Changbom Park, whose insights and persistence makes the novel method becomes reality. XDL acknowledges the supported from NSFC grant (No. 11803094). QGH is supported by grants from NSFC (grant No. 11335012, 11575271, 11690021, 11747601), the Strategic Priority Research Program of Chinese Academy of Sciences (Grant No. XDB23000000), Top-Notch Young Talents Program of China, and Key Research Program of Frontier Sciences of CAS.

Based on observations obtained with Planck (<http://www.esa.int/Planck>), an ESA science mission with instruments and contributions directly funded by ESA Member States, NASA, and Canada.

Funding for SDSS-III has been provided by the Alfred P. Sloan Foundation, the Participating Institutions, the National Science Foundation, and the U.S. Department of

Energy Office of Science. The SDSS-III web site is <http://www.sdss3.org/>. SDSS-III is managed by the Astrophysical Research Consortium for the Participating Institutions of the SDSS-III Collaboration including the University of Arizona, the Brazilian Participation Group, Brookhaven National Laboratory, Carnegie Mellon University, University of Florida, the French Participation Group, the German Participation Group, Harvard University, the Instituto de Astrofísica de Canarias, the Michigan State/Notre Dame/JINA Participa-

tion Group, Johns Hopkins University, Lawrence Berkeley National Laboratory, Max Planck Institute for Astrophysics, Max Planck Institute for Extraterrestrial Physics, New Mexico State University, New York University, Ohio State University, Pennsylvania State University, University of Portsmouth, Princeton University, the Spanish Participation Group, University of Tokyo, University of Utah, Vanderbilt University, University of Virginia, University of Washington, and Yale University.

REFERENCES

- Ade, P.A.R., Aghanim, N., & Arnaud, M., et al. arXiv:1502.01589
 Aghamousa, A., 2016, arXiv:1611.00036
 Alam, S., Ata, M., & Bailey, S., et al. 2016, submitted to MNRAS (arXiv:1607.03155)
 Albrecht, A., Bernstein, G., & Cahn, R., et al. 2006, [astro-ph/0609591].
 Alcock, C., & Paczynski, B. 1979, *Nature*, 281, 358
 Anderson, L., Aubourg, É., & Bailey, S. et al. 2014, MNRAS, 441, 24
 Ballinger, W.E., Peacock, J.A., & Heavens, A.F. 1996, MNRAS, 282, 877
 Bernstein, G. M. 1994, ApJ, 424, 569
 Betoule, M., Kessler, R., & Guy, J., et al. 2014, A&A, 568, 32
 Beutler, F., Blake, C., & Colless, M., et al. 2011, MNRAS, 416, 3017
 Blake, C., Glazebrook, K., & Davis, T. M., 2011, MNRAS, 418, 1725
 Chevallier, M., Polarski, D. 2001, Int. J. Mod. Phys. D, 10, 213
 Dawson, K.S., Schlegel, D.J., & Ahn, C.P., et al. 2012, AJ, 145, 10
 Efsthathiou, G. 2014, MNRAS, 440, 1138
 Eisenstein, D.J., Weinberg, D.H., & Agol, E., et al. 2011, AJ, 142, 72
 Hill, G. J., Gebhardt, K., Komatsu, E., et al. 2008, in *Astronomical Society of the Pacific Conference Series*, Vol. 399, *Panoramic Views of Galaxy Formation and Evolution*, ed. T. Kodama, T. Yamada, & K. Aoki, 115
 Hong, S.E., Park, C., & Kim, J. 2016, ApJ, 823, 103
 Jackson, J., 1972, MNRAS, 156, 1
 Jennings, E., Baugh, C.M., & Pascoli, S. 2011, MNRAS, 420, 1079
 Kim, J., Park, C., L'Huillier, B., & Hong, S. E. 2015, JKAS, 48, 213
 Kitaura, F.S., Rodríguez-Torres, S., Chuang, C.-H., et al. arXiv:1509.06400
 Klypin, A., Yepes, G., Gottlober, S., Prada, F., & Hess, S. 2016, MNRAS, 457, 4340
 Komatsu, E., Smith, K. M., & Dunkley, J., et al. 2011, ApJS, 192, 18
 Laureijs, R., Amiaux, J., & Arduini, S., et al. 2011, arXiv:1110.3193
 Lavaux, G., & Wandelt, B.D. 2012, ApJ, 754, 109
 Lewis, A., & Bridle, S. 2002, Phys. Rev. D, 66, 103511
 Li, M., Li, X.-D., Wang, S., & Wang, Y. 2011, Commun. Theor. Phys., 56, 525
 Li, X.-D., Park, C., Forero-Romero, J., & Kim, J. 2014, ApJ, 796, 137
 Li, X.-D., Park, C., Sabiu, C.G., & Kim, J. 2015, MNRAS, 450, 807
 Li, X.-D., Park, C., & Sabiu, C.G., et al. 2016, ApJ, 832, 103
 Li, X.-D., Sabiu, C.G., & Park, C., et al. 2018, ApJ, 856, 88
 Linder, E.V. 2003, Phys. Rev. Lett., 90, 091301
 Mao, Q., Berlind, A.A., Scherrer, R.J., et al. 2016, submitted to ApJ
 Marinoni, C., & Buzzi, A. 2010, *Nature*, 468, 539
 Matsubara T., & Suto, Y. 1996, ApJ, 470, L1
 Miao H., & Huang Z., 2018, ApJ, 868, 20
 O'Connell, R., Eisenstein, D., Vargas, M., Ho, S., & Padmanabhan, N. 2016, MNRAS, 462, 3
 Outram, P.J., Shanks, T., Boyle, B.J., Croom, S.M., Hoyle, F., Loring, N.S., Miller, L., & Smith, R.J. 2004, MNRAS, 348, 745
 Park, C., & Kim, Y.-R. 2010, ApJL, 715, L185
 Perlmutter, S., Aldering, G., & Goldhaber, G., et al. 1999, ApJ, 517, 565
 Reid, B., Ho, S., & Padmanabhan, N., et al. 2016, MNRAS, 455, 1553
 Riess, A.G., Filippenko, A.V., & Challis, P., et al. 1998, AJ, 116, 1009
 Riess, A.G., Macri, L., & Casertano, S., et al. 2011, ApJ, 730, 119
 Ross, A.J., Samushia, L., & Howlett, C., et al. 2015, MNRAS, 449, 835
 Ryden, B.S. 1995, ApJ, 452, 25
 Smeed, S.A., Gunn, J.E., & Uomoto, A., et al. 2013, AJ, 146, 32
 Weinberg, S. 1989, *Reviews of Modern Physics*, 61, 1
 Weinberg, D.H., Mortonson, M.J., Eisenstein, D.J., et al. 2013, *Physics Reports*, 530, 87
 Yoo, J., & Watanabe, Y. 2012, *International Journal of Modern Physics D*, 21, 1230002
 York, D.G., Adelman, J., & Anderson, J.E., et al. 2000, AJ, 120, 1579
 Zehavi, I., Zheng, Z., & Weinberg, D.H., et al. 2011, ApJ, 736, 59
 Zhang, X., Huang, Q.-G., & Li, X.-D., 2019, MNRAS, 483, 1655